***Highlights**

- Pyrochlores-based material presented for higher alcohol synthesis from synthesis gas
- Pyrochlores have the unique ability to produce bimolecular coupling of Rh and $Rh^{+}$
- Pyrochlores with ionic $Rh^{+}$ surface species show excellent ethanol selectivity

***Graphical Abstract**

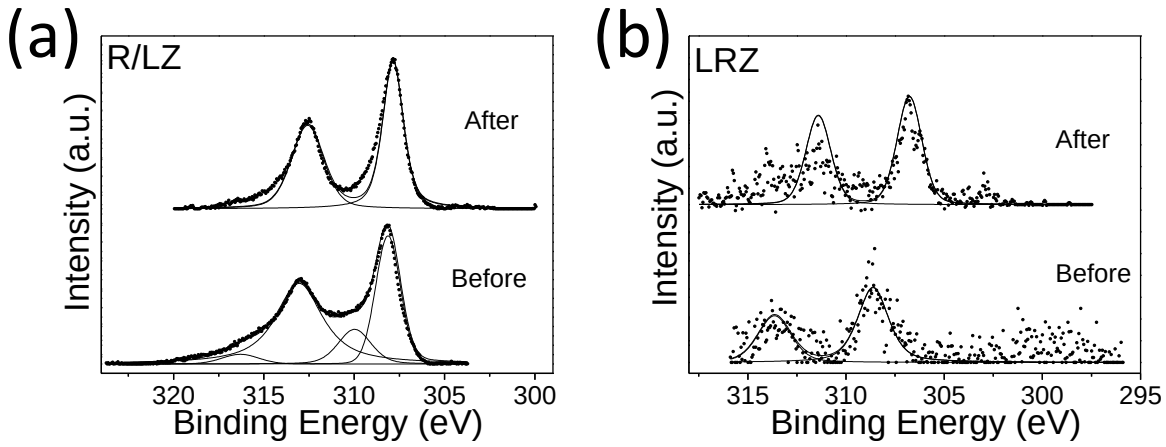

# Synthesis and Characterization of Rh-based Pyrochlores for Higher Alcohol Synthesis

Victor Abdelsayed[1,2], Dushyant Shekhawat[1], James A. Poston Jr.[1], James J. Spivey[1,3]

[1]National Energy Technology Laboratory, U.S. Department of Energy, 3610 Collins Ferry Rd., Morgantown, WV 26507, USA

[2]URS Corporation, 3610 Collins Ferry Rd., Morgantown, WV 26507, USA

[3]Louisiana State University, Department of Chemical Engineering, Baton Rouge, LA 70803, USA

## ABSTRACT

Two lanthanum zirconate pyrochlores ($La_2Zr_2O_7$; LZ) were prepared by Pechini method and tested for higher alcohols selectivity. In one, Rh was substituted into the pyrochlore lattice (LRZ, 1.7 wt%) while for the second, Rh was supported on an unsubstituted $La_2Zr_2O_7$ (R/LZ, 1.8 wt%). X-ray photoelectron spectroscopy (XPS) and temperature programmed reduction (TPR) results show that the surface reducibility depends on whether the Rh is in (or supported on) the LZ pyrochlore. Rhodium in the LRZ is more reducible than rhodium supported on the R/LZ pyrochlore, likely due to the presence of a perovskite phase (LaRhO3; identified by XRD), in which rhodium is more reducible. The formation of the perovskite accompanies that of the pyrochlore. CO hydrogenation results show higher ethanol selectivity for R/LZ than LRZ, possibly due to the strong interaction between Rh and LZ on the R/LZ, forming atomically close $Rh^+/Rh^0$ sites, which have been suggested to favor ethanol production.

*Keywords:*

*Higher alcohol synthesis, Pyrochlore, CO hydrogenation, syngas conversion, ethanol synthesis, Pechini method*

## 1.0 Introduction

The conversion of syngas from natural gas, coal, or biomass into $C_{2+}$ alcohols has attracted increasing attention due to the potential use of these oxygenates as neat fuels or fuel additives [1-3]. These compounds have higher energy density and are less corrosive to the fuel infrastructure than methanol. The stoichiometry of the higher alcohol synthesis reaction from syngas can be expressed as:

$$nCO + 2nH_2 \rightarrow C_nH_{2n+1}OH + (n-1)H_2O;\ \Delta H < 0 \text{ and } n = 2\text{-}8$$

The major byproducts are $C_1$ compounds, including methanol, and the thermodynamically favored products $CO_2$ and methane [1, 4]. Therefore, the major challenge for higher alcohol synthesis from syngas is to develop a catalyst with high kinetic selectivity towards higher alcohols, specifically catalysts that drive the reaction toward the formation of the C-C bond.

Rh catalysts are extensively studied for their ability to produce alcohols via hydrogenation of CO [5-7], $CO_2$ [1, 8-9] or both [2, 10-11]. Literature shows that the activity and selectivity of Rh-based catalysts are increased by promoter(s) [12-14], choice of support [5, 15-17], synthesis method [18-19], and Rh precursors [20]. In general, the optimum higher alcohol catalyst should have a balanced rate of CO dissociation, hydrogenation and CO insertion [21-23]. For example, promoters such as rare earth metals [23-24], alkali metals [25-26], and other transition metals [23, 27-28] play an important role in these elementary steps. Usually, these promoters are used to polarize the oxygen atom of the absorbed CO molecule and hence weaken the C-O bond, leading

to CO dissociation followed by a hydrogenation step to form $CH_x$ species. CO insertion and hydrogenation is then necessary to produce the final higher alcohol products.

In addition to promoters, optimizing the chemical and the electronic nature of Rh species on the surface could improve the activity and selectivity to higher oxygenates. However, there are some contradictory results on the electronic state of Rh active sites in the literature. While Watson and Somorjai [29] claimed that oxidized Rh species in perovskite ($LaRhO_3$) correlate with ethanol high selectivity and are associated with the stabilization of $Rh^{n+}$ on the surface, Gysling et al. [30] showed that oxygenate formation occurs on metallic Rh sites in $LaRhO_3$.

Recently, the presence of an atomically adjacent ionic and metallic Rh species ($Rh^0$-$Rh^{n+}$) has been reported [20, 31-32] to enhance the coupling between CO and $CH_x$ and the selective formation of ethanol via ketene [33-34] ($H_2C=C=O$) or acetyl [33, 35] ($H_3C=C=O$) intermediates. For example, Du et al. [24] show that a surface complex such as Figure 1a enhances higher oxygenate selectivity via the formation of a “tilted” CO species in which both the carbon and oxygen atoms are bound to the surface (P could be a promoter cation or an oxygen vacancy)

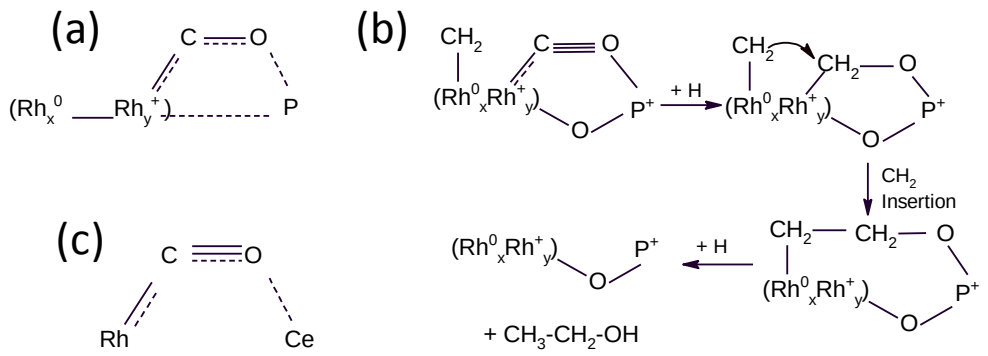


Figure 1. (a) Postulated Rh sites corresponding to higher oxygenate selectivity [24], (b) Mechanism of ethanol formation on promoted Rh [35], and (c) activation of CO on Rh/ceria surface, leading to increased higher oxygenate selectivity [36].

A similar $Rh^o$---$Rh^{n+}$ pair has been postulated by Wang et al. [35]. They also suggest that a metal promoter (Mn in their case) is in atomic proximity to the $Rh^{n+}$ atom, forming a "tilted" CO, bound such as the one postulated by Du et al. [24] in Figure 1a. They show that ethanol is formed by insertion of a carbene from the $Rh^o$ site, as shown in Figure 1b.

In the case of the Rh-substituted zirconate (LRZ) , it is possible in principle that the type of $Rh^o$---$Rh^{n+}$ sites shown here could be formed by the proximity of an $Rh_y^{1+}$ site (produced by Rh atoms closely associated with lattice oxygen on the pyrochlore surface) and an $Rh^o$ site in a rhodium cluster on the surface. Additionally, rhodium supported on $La_2Zr_2O_7$ was used to determine the difference between rhodium within the pyrochlore, and rhodium supported on the pyrochlore.

Based on FTIR results, another type of site, shown in Figure 1c, has been proposed by Kiennemann et al. to account for the formation of higher oxygenates [36]. This site consists of a Rh-Ce site which also binds CO through both the oxygen and carbon atoms. This is postulated to

lead to the formation of a formyl intermediate by hydrogenation of the activated CO (presumably through $H_2$ dissociation on the Rh site), which they show to be a key intermediate in the formation of higher oxygenates. However, Kiennemann et al. also note that this is not the only possible consequence of CO activation on this type of site, which may either favor CO dissociation (by diminishing the carbon-oxygen bond order), or promote CO insertion (by modifying the electron density of the carbon atom). It is not clear whether this sort of site would uniquely favor one or the other of these options. This sort of site may be formed at the surface of a Rh-substituted lanthanum zirconate pyrochlore surface (where the role of Ce is taken by surface lanthanum sites), suggesting that such a pyrochlore may have increased selectivity to higher oxygenates. In this case, no Rh metal beyond that in the pyrochlore structure would be necessary to produce this type of site.

In the present work, we report CO hydrogenation on three catalysts:

(a) Rh substituted into the zirconate site (LRZ), with Rh atomically bound to oxygen and lanthanum at the surface;
(b) Rh supported on the pyrochlore (R/LZ), with no covalent bond between the Rh atoms and the pyrochlore; and
(c) Lanthanum zirconate (LZ) as a baseline catalyst.

LRZ and R/LZ are intended to have different types of Rh-pyrochlore interaction; specifically, in LRZ all rhodium catalysts are closely associated with the pyrochlore lattice, while on R/LZ, at least some rhodium is presumably more metallic since it is not in the pyrochlore lattice. The goal is to investigate systematically the role of these Rh species on the synthesis of higher oxygenates.

## 2.0 Experimental

### 2.1 Catalyst synthesis

#### *2.1.1 Materials*

Zirconium oxynitrate ($ZrO(NO_3)_2.xH_2O$), lanthanum nitrate hexahydrate ($La(NO_3)_3.6H_2O$), anhydrous citric acid ($C_6H_8O_7$), ethylene glycol ($C_2H_6O_2$), rhodium chloride ($RhCl_3$), rhodium nitrate ($Rh(NO_3)_3.xH_2O$), hydrazine monohydrate ($N_2H_4.H_2O$), and analytical grade ethanol (EtOH) were purchased from Alfa Aesar and were used without any further purification.

#### *2.1.2 Rh-substituted pyrochlores*

Pyrochlores of lanthanum zirconate (LZ) and 2 wt% Rh-substituted lanthanum zirconate (LRZ) catalyst materials were prepared using a modified Pechini method [37-38]. Typically, citric acid (CA), a metal complexing agent, was added to a mixed aqueous solution of lanthanum nitrate, zirconium oxynitrate, and rhodium chloride to form a clear solution. The molar ratio between CA and total metal ions was kept at 1.2. The clear solution was heated to $70^oC$ on a stirred hot plate before ethylene glycol (EG) was added such as the molar ratio of EG to CA is unity. The solution was kept under stirring at this temperature for several hours to evaporate water and accelerate polymerization between metal-chelated citric acid and ethylene glycol. A clear viscous gel was obtained, which was further heated in a heating mantle at $130^oC$ until an amorphous polyester-type resin was obtained. The solid material was collected and calcined at $1000^oC$ for 8 hours to breakdown the organic polymer and burns the carbon off leading to a highly crystalline mixed metal oxide material.

### *2.1.3 Rh-deposited pyrochlores*

Microwave-assisted chemical reduction method was used to deposit 2wt% Rh on the surfaces of pure un-substituted (LZ)-pyrochlore catalysts (prepared by modified Pechini method mentioned in Section 2.1.2). In a typical procedure, rhodium nitrate was dissolved in a 100 ml of a $H_2O$:EtOH (1:2) mixture such as the Rh metal content in this solution is equivalent to 2wt% Rh (to be deposited on the LZ pyrochlore catalyst). The LZ powder was dispersed in the above mentioned solution for 3 hours then hydrazine monohydrate (500μl) was added quickly at room temperature under vigorous stirring. No color change was observed to the dispersion indicating that the Rh ions did not reduce under room temperature conditions. The solution was kept under stirring for another hour before being transferred into a sealed Teflon vessel and placed on a turntable tray of an Anton Paar microwave reaction system (Synthos 3000) equipped with pressure and temperature sensors. The dispersion was microwaved for 5 min under continuous stirring and 800 W of microwave power. After cooling the dispersion, the particles were separated by centrifuge, washed with ethanol and then dried under vacuum at $10^{-3}$ torr for 48 hours.

## 2.2 Catalyst Characterization

### *2.2.1 X-ray Diffraction (XRD)*

Powder X-ray diffraction analysis was performed on a Panalytical X'pert Pro (PW3040) X-ray diffraction system utilizing Cu Kα radiation. Samples were placed on a zero diffraction Si holder and were scanned from 10 to 90° (2θ). ). Analysis was carried with Highscore Plus Analysis software equipped with a standard ICDD X-ray diffraction database supplied by Panalytical. Average crystallite size was calculated from the diffraction pattern using Scherrer equation [39]

*($d = k\lambda/(B\cos\theta)$* where *d* is the average crystallite size, *k* is a constant that depend on crystallite shape, $\lambda$ is the x-ray wavelength, $\theta$ is the diffraction angle, and *B* is the FWHM (full width at half max) of the diffraction peak.

### *2.2.2 Surface area and ICP analysis*

The specific surface area was calculated from the $N_2$ isotherm data using the Brunauer-Emmett-Teller (BET) model (P/Po = 0.1-0.3). The data were collected using a Micromeritics ASAP 2020 unit. Prior to analysis, the samples were first degassed at 300$^{o}$C for 3 hours before being cooled to room temperature for analysis. The Barrett, Joyner, and Halenda (BJH) model was used to estimate the pore size of the catalysts [40]. The bulk concentrations of La, Zr, and Rh were determined by inductively coupled plasma optical emission spectrometer (ICP-OES) manufactured by PerkinElmer (Optima 7300). Acid-digestion techniques were used to dissolve the catalysts prior to the ICP analysis.

### *2.2.3 Temperature programmed reduction (TPR) and $H_2$ pulse chemisorption*

TPR and $H_2$ pulse chemisorption experiments were carried out using a flow system with a thermal conductivity detector (Micromeritics Autochem 2910). Prior to each TPR run, the catalysts (~0.2g) were heated to 950 $^{o}$C under 5 % $O_2$/He (50 ml/min, ramp 5 °C/min). After the catalyst cools down to 50 $^{o}$C, the TPR analysis was then carried out by ramping the temperature to 950$^{o}$C (5°C/min) under 5.0% $H_2$/Ar (30 ml/min).

$H_2$ pulse chemisorption was used to determine the percentage of Rh metal dispersed on the surface of reduced catalyst at 50$^{o}$C. First the catalyst was purged with Ar gas (50 ml/min) at

50$^{o}$C after being reduced in $H_2$/Ar at 950 $^{o}$C then 5.0% $H_2$/Ar gas pulses each of 0.5377 ml was introduced to the sample until hydrogen saturate the catalyst surface. The Rh metal dispersion was calculated using the actual ICP concentration of Rh.

### *2.2.4 X-ray photoelectron spectroscopy (XPS)*

The elemental electronic states of the catalyst surface were investigated using XPS. The measurements were carried out on a Physical Electronics (PHI) spectrometer model 590. The photoelectron kinetic energy was measured by OmniFocus III spherical capacitance analyzer (SCA). Magnesium anode was used as the source of X-ray radiation (MgK$\alpha$ : 1253.6 eV).The pressure in the analysis chamber was maintained between$10^{-8}$ to $10^{-9}$Torr during measurements. The binding energies were corrected utilizing the reference binding energy (BE) of adventitious carbon $C_{1s}$ at 284.8 eV. The spectra from the regions related to $Zr_{3d}$, $La_{3d}$, $Rh_{3d}$, $C_{1s}$, and $O_{1s}$ core levels were recorded and analyzed using "Auger-Scan" analysis software developed by RBD Instruments for each sample.

### *2.2.5 Electron microscopy and X-ray microanalysis*

Transmission electron microscopy (TEM) was conducted on JEOL JEM-2100 operated at accelerating voltages of 200 kV and equipped with a high resolution CCD camera. Samples were prepared by placing a droplet of ethanol-dispersed particles on a Formvar carbon-coated, 300-mesh copper grid (Ted Pella) and allow it to evaporate in air at room temperature. Energy dispersive spectroscopic (EDS) analysis was obtained utilizing a JEOL FE-7600 scanning electron microscope (SEM) interfaced to a Thermo-Electron Noran System Seven (NSS) X-ray microanalysis system. The EDS detector utilized in the X-ray microanalysis was a Thermo-

Electron Ultradry Energy dispersive spectrometer, which was calibrated utilizing the Cu Kα line at 8.041 kV.

### 2.3 Catalyst activity measurements

#### *2.3.1 Experimental setup and reaction conditions*

A continuous fixed-bed flow reactor was used to measure the catalytic performance of the catalysts (Figure 2). Table 1 shows the reaction conditions used in the CO hydrogenation reaction over Rh-based pyrochlore catalysts. In a typical run, the catalyst (1g) was first ground, then diluted with sand (5 g) and then placed in the reactor before being *in-situ* reduced under 10% $H_2/N_2$ flow (500 sccm) at 500 $^oC$ for 2 hours at atmospheric pressure. Once the reactor was cooled down to the desired reaction temperature (280 $^oC$), the pressure was adjusted to 2.9 MPa and the syngas mixture ($H_2/CO$ =2) was introduced.

Table 1. Reaction conditions used to screen Rh-based pyrochlore catalysts

| Reaction conditions | Parameter | Value |
|---|---|---|
| | $H_2/CO$ | 2 |
| | T ($^oC$) | 280 |
| | P (MPa) | 2.9 |
| | WHSV (cc/h/$g_{cat}$) | 15,000 |
| | Cat. wt. (g) | 1.0 |

*2.3.2 Product analysis*

Oxygenates in the product gas steam (methanol, ethanol, n-propanol, isopropanol, isobutanol, n-butanol, acetone, and acetaldehyde) were separated and analyzed in Hewlett Packard 5890 Gas Chromatograph (GC) equipped with FID detector and Restek-StabilwaxDA column (60m, 0.32mm ID). The GC data were processed using TotalChrom Workstation software. Hydrocarbons and other outlet gases ($H_2$, CO, $CO_2$, and $CH_4$) were analyzed by a ThermoONIX model Prima δB Mass Spectrometer equipped with an electron impact ionization source. The MS analysis of the products was conducted after condensing out any oxygenates in the gas stream using a sample conditioner connected in series with the MS as shown in Figure 2. The MS and GC were calibrated with the appropriate standard gas mixtures before each run. The CO conversion, in all reactions studied, was kept intentionally under 1% to avoid any possible oxygenate condensation before analysis and to ensure that the produced oxygenates remain in the vapor phase prior to GC injection port. The GC column (polar polyethylene glycol (PEG) columns) used in the study is not designed to handle high concentrations of water, one of the CO hydrogenation side products. The product selectivity was calculated based on carbon efficiency and is defined as:

$$S\ (\%) = \ 100\ \mathrm{x}\frac{n_i C_i}{\sum(n_i C_i)}$$

where $n_i$ and $C_i$ is the number of carbon atoms and molar concentration of the $i^{th}$ product, respectively.

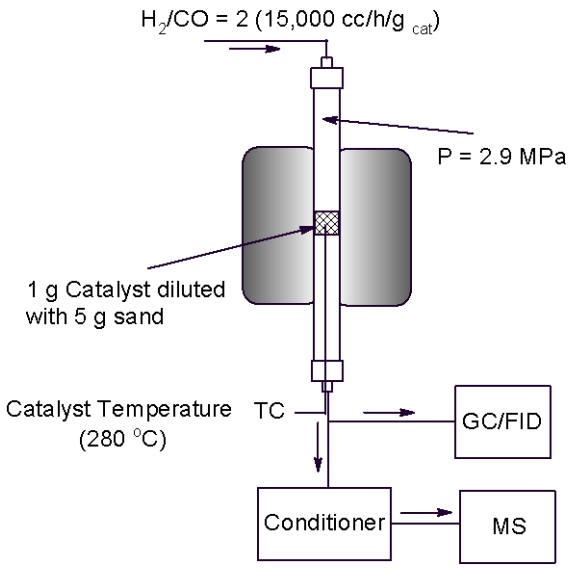


Figure 2. Experimental setup used for CO hydrogenation reaction into higher alcohols.

## 3.0 Results and discussion

### 3.1 Catalyst characterization

#### 3.1.2 XRD analysis

The powder X-ray diffraction patterns for fresh-calcined LZ, Rh-deposited LZ, and Rh-substituted LZ catalysts are shown in Figure 3a-c. Only a single crystalline phase, identified as $La_2Zr_2O_7$ (JCPDS:17-0450) was observed in LZ catalyst. The diffraction peaks located at $2\theta$= 28.63, 33.15, 47.61, and 56.45$^o$ correspond to diffraction from [222], [400], [440], and [622] crystal planes respectively, with a face centered cubic unit cell structure [41-42]. When 1.7 wt% Rh was substituted in the catalyst material, new diffraction peaks at $2\theta$ = 31.88 and 45.71$^o$ corresponding to $LaRhO_3$ perovskite (JCPDS:10-0305) were observed in addition to the main pyrochlore peaks. The formation of perovskite phase could be due to the presence of excess Rh that could not substituted in the B-site of pyrochlore [43-44] possibly due to the mismatch between the ionic radii of Rh and Zr cations ($r_{Rh} < r_{Zr}$). Another possibility is that these

perovskite secondary peaks maybe formed during the calcination process[45-46]. The catalysts were calcined for 8 h at 1000$^{o}$C in air which could leading to the formation of $LaRhO_3$ [45-46]. No other metal oxides of La, Zr, or Rh were observed in the XRD patterns indicating that the Pechini method produces a homogeneous mixed metal oxide phases with no single metal oxide segregations. The average pyrochlore crystal sizes in LZ and LRZ were determined from the XRD patterns parameters according to Scherrer equation to be very similar (30±3 nm), while the perovskite crystal size was smaller (19±2 nm).

Rh nanocrystals were deposited on the surfaces of LZ catalyst by microwave-assisted chemical reduction method. Microwave irradiation (MWI) provides a fast dielectric heating, due to the difference in the reactant and solvent dielectric constants, leading to enhancement in the reduction rate of Rh nitrate by hydrazine hydrate [47-49]. A microwave-induced homogeneous nucleation of metal clusters is intended to produce a narrow size distribution of Rh on the catalyst surfaces. The XRD patterns for Rh deposited pyrochlore catalysts (calcined in air at 500 $^{o}$C) are also shown in Figure 3b. No size change in the pyrochlore particles was observed before and after Rh deposition with no diffraction peaks corresponding to Rh metal or its oxide being observed. This could be due to several factors, such as size, concentration and dispersion of Rh metal particles. In this case, only 1.7 wt% Rh was deposited on the pyrochlore, which could be beyond the detectable limits of XRD, especially if these Rh nanocrystals are highly dispersed and less than ~3 nm in diameter.

Figures 3d and 3e show the XRD patterns for LRZ catalysts collected after temperature programmed reduction (TPR) and CO hydrogenation reaction, respectively. No change in the

diffraction peaks of pyrochlore phase were observed after being subjected to these reduction conditions. However, the perovskite diffraction peaks completely disappeared due to reduction of $LaRhO_3$ into Rh and $La_2O_3$ at high temperature by $H_2$ or $CO/H_2$ [30]. It is not clear whether the perovskite-Rh particles are incorporated into the pyrochlore structure or remained on the surface. In both cases, the XRD could not differentiate between these two possibilities due to the small concentration of Rh (1.8 wt%).

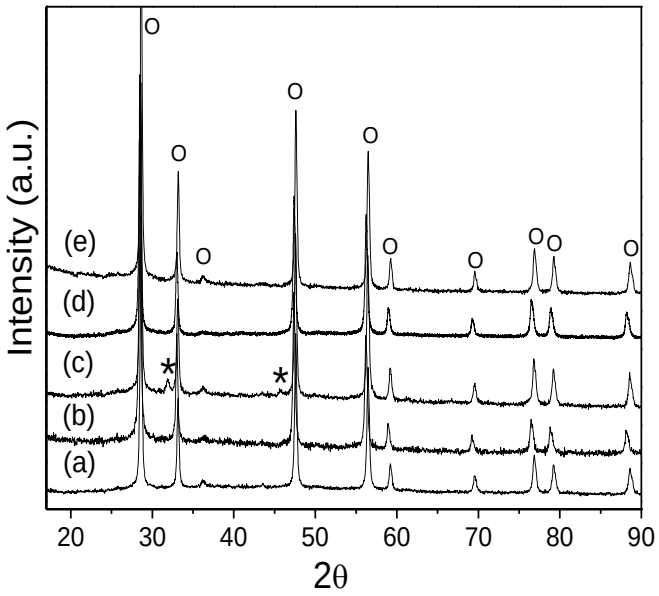


Figure 3. X-Ray diffraction patterns for (a) calcined LZ, (b) calcined R/LZ, (c) calcined LRZ, (d) reduced LRZ after TPR, and (e) spent LRZ after CO hydrogenation reaction. (O) for pyrochlore and (*) for perovskite crystalline phase peaks.

### 3.1.1 Surface area and Rh metal dispersion

The catalyst specific BET surface area, total pore volume and average pore diameter are reported in Table 2 for freshly calcined materials. Depositing Rh on LZ (R/LZ) increased the BET surface area slightly, from 5.31 ± 0.03 $m^2/g$ to 6.26 ± 0.01 $m^2/g$. This is possibly due to the formation of

Rh nanocrystals on the surface leading to a higher total surface area per unit weight compared to pure LZ catalyst. However, for LRZ, the surface area was essentially the same as for LZ, as expected if rhodium is isomorphically substituted into the LZ lattice. The average pore diameter of the R/LZ was slightly lower than that of the LZ or LRZ catalysts, which is consistent with the formation of rhodium clusters in the pores of the R/LZ.

The bulk Rh content and its metal dispersion percentage on the surface are displayed in Table 2. The ICP analysis showed that both LRZ and R/LZ catalysts had a similar bulk concentration of Rh at 1.7 and 1.8 wt%, respectively. After both LRZ and R/LZ were subjected to TPR at 950 $^{o}$C, the Rh substituted pyrochlore catalyst (LRZ) shows a higher Rh dispersion (10.3%) than R/LZ (6.0%). The reducible and accessible Rh on the R/LZ is apparently less than for the presumably atomically disperse rhodium on the exposed surface of LRZ, despite the fact that most of the rhodium in the LRZ catalyst resides within the crystalline lattice, not on the surface.

Table 2. Surface properties and Rh metal dispersion of fresh pyrochlore catalysts

| **Catalyst** | **BET Surface area ($m^2/g$)** | **Total pore volume (cc/g) x $10^3$** | **Average pore diameter (nm)[a]** | **Rh loading (wt%)[b]** | **Rh dispersion (%)[c]** |
|---|---|---|---|---|---|
| **LZ** | 5.31 ± 0.03 | 44.9 ± 0.70 | 34.8 ± 0.89 | -- | -- |
| **R/LZ** | 6.26 ± 0.01 | 44.3 ± 0.38 | 29.5 ± 0.26 | 1.8 | 6.0 |
| **LRZ** | 5.64 ± 0.02 | 45.1 ± 2.48 | 32.0 ± 2.08 | 1.7 | 10.3 |

[a]The Barrett, Joyner, and Halenda (BJH) model [40] was used to estimate the pore size of the catalysts.
[b]The Rh loading was determined using ICP-OES technique.
[c]The Rh metal dispersion on the catalyst surfaces was determined by $H_2$ pulse chemisorption technique after performing a TPR at 950$^{o}$C.

### 3.1.3 Temperature programmed reduction (TPR)

Figure 4 displays the TPR results for calcined pyrochlore catalysts. A negligible broadening due to LZ reduction was barely noticeable at the same scaling, specially at high temperature reduction (450-600 $^{o}$C), consistent with what have been observed in the literature by Haynes [50] and by Hoang [51]. This indicates that the La and Zr mixed oxide species are very stable under reduction conditions and high temperatures. When Rh was deposited on LZ catalyst (R/LZ), a weak reduction peak appeared around 253$^{o}$C which can be assigned to the Rh species on the LZ surface. This reduction peak temperature is much higher than that observed for Rh supported on $SiO_2$ and $Al_2O_3$ catalysts (70-136$^{o}$C) [23, 52-53], suggesting a strong Rh-pyrochlore interaction. This may be attributed to the LZ structure, which has high oxygen ion conductivity [54], and may stabilize small Rh clusters on the surface.

Table 3 shows that the overall hydrogen consumption is less for the R/LZ than the LRZ; even though the bulk weight loading of the two is essentially equal This suggests that the small Rh clusters on the surface are unexpectedly stable to reduction on the pyrochlore surface, consistent with the dispersion results (Table 2) showing significantly more surface reducible rhodium in the LRZ than that in the R/LZ. .

For LRZ, a major reduction peak around 430 $^{o}$C was observed, suggesting that rhodium is part of lattice and it is not simply supported on the surface. This broad peak had two components, a lower temperature shoulder at around 380 $^{o}$C followed by a higher temperature peak at around 429 $^{o}$C. This indicates two different forms of rhodium on the surface each with different coordination environment. This may be due to Rh being substituted in both the pyrochlore and

perovskite crystal structures. This would explain both the presence of two overlapping reduction peaks in the TPR profile, and the fact that they are close to one another, as would be expected for a pyrochlore and perovskite.

The total $H_2$ uptake is far greater for LRZ (0.28 mg $H_2/g_{cat}$) than for R/LZ (0.07 mg $H_2/g_{cat}$) indicating the higher stability of Rh species on the R/LZ. The maximum calculated $H_2$ uptake was calculated for both catalysts (Table 3) to be 0.66 and 0.70 mg $H_2/g_{cat}$ using the ICP concentration of Rh (Table 2) and assuming a complete reduction of Rh with the highest oxidation state ($Rh^{4+}$). The reducible fraction of Rh was calculated to be 42 and 10% for LRZ and R/LZ, respectively.

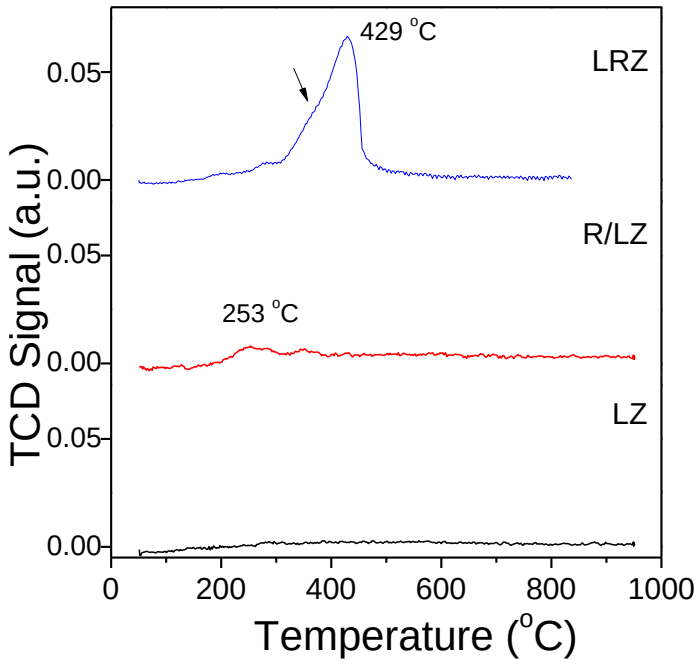


Figure 4. TPR profiles for freshly calcined pyrochlore-based catalysts.

Table 3. Catalysts reducibility obtained from TPR analysis for fresh, calcined catalysts

| **Catalyst** | **Total $H_2$ uptake** | | |
|---|---|---|---|
| | Experimental* | Calculated** | Estimated Fraction of reduced Rh |
| | (mg $H_2/g_{cat}$) | | (%) |
| **LZ** | 0.02 | -- | -- |
| **R/LZ** | 0.07 | 0.70 | 10 |
| **LRZ** | 0.28 | 0.66 | 42 |

* *Based on TPR measurements*
** *Based on the ICP concentration of Rh in the catalyst and the assumption of complete reduction of Rh species ($RhO_2 + 2H_2 \rightarrow Rh + 2H_2O$)*

### 3.1.4 X-ray photoelectron spectroscopy (XPS)

The XPS spectra for fresh and spent catalysts were displayed in Figure 5. The spent catalyst was reduced at 500 $^oC$ under 10% $H_2/N_2$ before CO hydrogenation reaction took place at 280 $^oC$. The intensity of the $Rh_{3d}$ XPS spectra for Rh-deposited catalyst (R/LZ) is much greater than that observed for Rh-substituted catalyst (LRZ) due to the nature, location and concentration of Rh species on the surfaces found in these catalysts. This observation also agrees with the preparation method adopted to introduce Rh species to the catalyst (substituted versus deposited catalysts).

Peaks at binding energies (BE) between 308.17 to 309.43 eV and between 312.92 to 314.52 eV are assigned to Rh $3d_{5/2}$ and $3d_{3/2}$ regions, respectively [55-56]. The spectra shows that the Rh 3d peaks are shifted to lower binding energies after CO hydrogenation due to the reduction of the Rh species on the surface. The difference in Rh $3d_{5/2}$ binding energy ($\Delta$BE) before and after CO hydrogenation reaction is reported in Table 4. The $\Delta$BE significantly increased from R/LZ to

LRZ: R/LZ (0.33 eV) < LRZ (2.06 eV). This indicates that LRZ is the more reducible catalyst. This could also imply that the interaction between Rh and lanthanum zirconate crystal structure is higher for R/LZ than for LRZ, possibly due to perovskite reduction in LRZ into metallic Rh and $La_2O_3$ [30]. The catalyst reducibility order obtained from XPS analysis agrees well with the total $H_2$ uptake per gram catalyst determined from the TPR analysis in Table 3. The broadening of the Rh 3d peaks observed in LRZ indicates the higher metal dispersion on the surface [57] compared to a less broad peaks for R/LZ catalyst. These results agree qualitatively with the $H_2$ pulse chemisorption data reported in Table 2.

Table 4 shows that the Rh $3d_{5/2}$ binding energy for freshly calcined catalysts are assigned to nonstoichiometric Rh oxide species ($Rh^{3+}$ and $Rh^{4+}$) [57-59] with more ionic nature as we move towards LRZ with a difference of binding energy of 0.29 eV between fresh R/LZ and LRZ catalysts. On the other hand, after reaction the binding energies of Rh $3d_{5/2}$ show that the LRZ has more metallic nature contribution while those for R/LZ still show some ionic nature contribution. For example, spent R/LZ catalyst has a peak at 307.84 eV which is assigned to a nonequimolar mixture of $Rh^o$ and $Rh^+$ [29-30, 57, 59]. These results indicate that La and Zr ions in the pyrochlore lattice could play a significant role in stabilizing $Rh^o$-$Rh^+$ species at the interface.

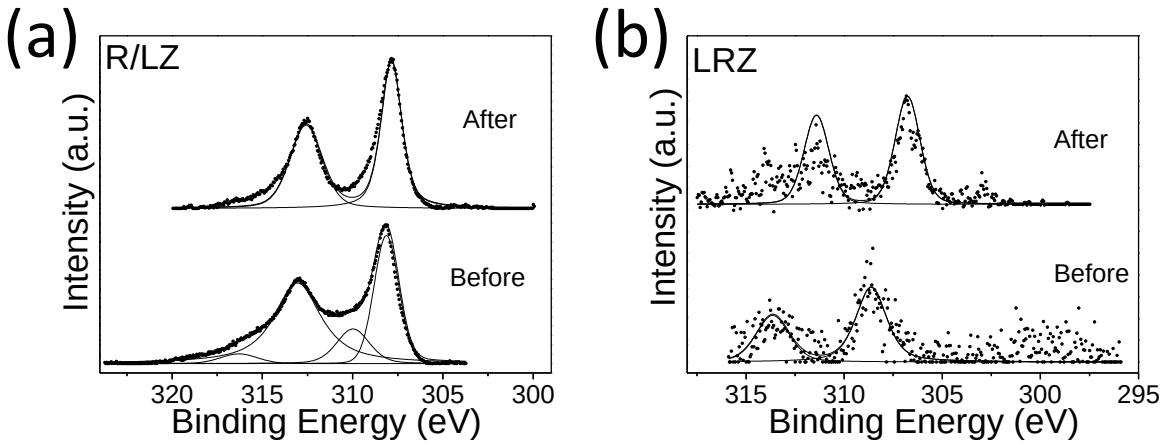


Figure 5. XPS for fresh and spent catalysts (Rh 3d region)

Table 4. XPS binding energies for Rh $3d_{5/2}$ of fresh and spent catalysts

| **Catalyst** | **Rh $3d_{5/2}$ (BE, eV)** | | |
|---|---|---|---|
| | **Fresh** | **Spent** | **ΔBE (eV)** |
| **R/LZ** | 308.17 | 307.84 | 0.33 |
| **LRZ** | 308.46 | 306.78 | 2.06 |

### 3.1.5 Transmission electron microscopy (TEM)

TEM was used to gain direct information about the size and structure of the prepared pyrochlore catalysts. Figure 6a shows the TEM image for the fresh calcined LZ catalyst. The average particle size is between 25-40 nm, which agrees well with the estimated values from the XRD data. Particles were found to be highly agglomerated with a secondary particle size in the micrometer scale range. These observations were also observed with Field emission Scanning electron microscopy (not shown here). After Rh (1.8 wt%) was deposited on the LZ surfaces, the particle surface morphology of calcined R/LZ changed, as observed from the TEM image shown

in Figure 6b. Disperse Rh nanoparticles of less than 2 nm were observed covering LZ catalyst. The TEM results confirm the presence of dispersed Rh nanocrystals on the LZ catalyst surface which could explain the absence of Rh peaks in the XRD patterns due to their small size, dispersion and concentration. The results also indicate that the MWI method employed to deposit Rh nanoparticles on the catalyst surface produces small Rh nanocrystals with narrow particle size distribution.

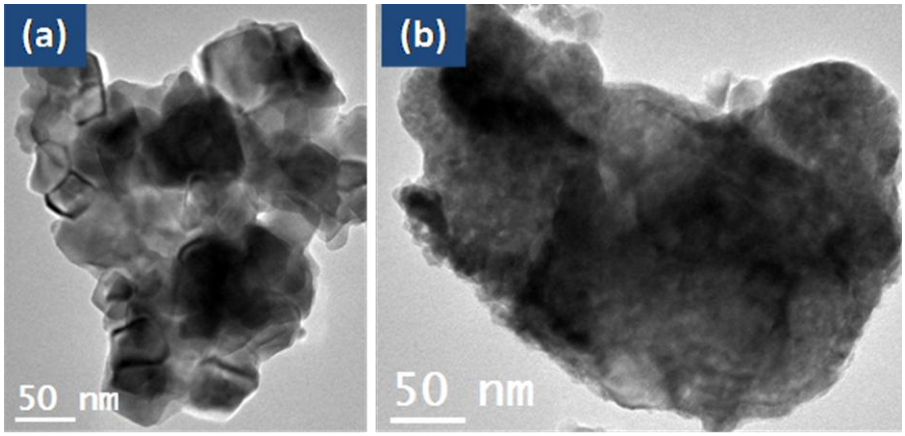


Figure 6. TEM images for LZ catalyst before (a) and after (b) Rh was deposited on the surface (R/LZ).

### 3.1.6 Bulk and surface composition

The compositional difference between substituted and deposited Rh-pyrochlore catalysts is shown in Table 5. The ICP bulk analysis showed that the atomic ratios for La/Zr and Rh/La are very similar for these two catalysts, with 1.1 and 0.049 for LRZ, and 1.0 and 0.053 for R/LZ, respectively. However, at the surface, EDX and XPS analysis show different atomic ratios with more La and Rh on the surface than in the bulk especially for R/LZ catalyst. The XPS Rh/La

ratio for R/LZ catalyst compared to that obtained by EDX shows much more Rh on the surface which is expected due to the penetration depth difference associated with these two techniques [60-62]. XPS has a shorter penetrating depth (~ 5 to 10 nm) while EDX has a longer one (1 to 10 μm) [60-62].

Table 5. Atomic ratios as determined by ICP, EDX, and XPS techniques as a function of Rh location in the catalyst

| **Atomic ratio** | **Technique** | **Catalyst** | |
|---|---|---|---|
| | | LRZ | R/LZ |
| **La/Zr** | ICP | 1.1 | 1.0 |
| | EDX | 1.3 | 1.2 |
| | XPS | 1.3 | 0.9 |
| **Rh/La** | ICP | 0.05 | 0.05 |
| | EDX | 0.07 | 0.10 |
| | XPS | 0.01 | 2.50 |

### 3.2 Catalytic activity measurements

Selectivities for CO hydrogenation for LZ, R/LZ, and LRZ catalysts are shown in Figure 7. The main products are methanol, ethanol, n-propanol, and methane. Only trace amounts of other oxygenates such as butanol, acetone, and acetaldehyde were detected, but only account for less than 1% selectivity collectively. For LZ, the results show no selectivity for alcohols. Methane and $CO_2$ were the major products observed with LZ catalyst. The absence of oxygenate formation on LZ confirms the essential role that Rh plays as an active catalyst for CO catalytic

hydrogenation into alcohols and other oxygenates [1, 63]. For LRZ and R/LZ, methanol, ethanol, and n-propanol were observed. The methanol to ethanol ratio was found to be the highest for LRZ catalyst, with values approaching 2.3 as compared to only 0.25 for R/LZ catalyst.

Figure 7 shows that R/LZ has the highest selectivity towards ethanol and the lowest selectivity towards methanol and $CO_2$.On the other hand, LRZ has approximately four times higher methanol selectivity with lower ethanol selectivity. The more metallic Rh nature on the surface of the LRZ ($Rh^o >> Rh^+$) correlate with its high methanol selectivity as were observed by Gysing et al. [30], while R/LZ, with more ionic Rh nature on the surface ($Rh^+ >> Rh^o$) has the highest ethanol selectivity. These results suggest that the electronic state of Rh catalyst on the surface and the relative ratio between $Rh^+/Rh^o$ species is a determining factor in the product selectivity and the C-C coupling mechanism. For these two catalysts, the $Rh^o/Rh^+$ ratio in the R/LZ leads to greater C-C bond formation and ethanol selectivity. This is consistent with the XPS results shown above, and with literature showing stabilized ionic $Rh^+$ decreases the rate of hydrocarbon formation while increasing that of oxygenate formation [55].

The methanol to ethanol ratio observed for LRZ and R/LZ is very similar to what has been reported for $LaRhO_3$ and $Rh/La_2O_3$ [24, 29]. The variation in product selectivity could be due to competing processes of hydrogenation and carbonylation corresponding to varying concentrations of molecular and dissociated CO and hydrogen on the surface. At the metal-support interface region of reduced R/LZ, the XPS results show that Rh binding energy (307.84 eV) is in between $Rh^o$ at about 307 eV and $Rh^{3+}$ at about 311 eV. This suggests the presence of Rh in two oxidation states: $Rh^o$ and $Rh^{n+}$. The proximity of these types of Rh atoms at the metal-

support interface region enhances the selectivity of $C_2$ and higher oxygenates, consistent with earlier studies [35-36]. .

The high ethanol to methanol ratio observed with R/LZ is consistent with XPS and TPR results which suggest a strong metal-support interaction between deposited Rh and LZ support. The interface between Rh and LZ appears to play an important role in maintain a rate balance between CO dissociation and CO insertion under hydrogenation conditions that favors the formation of higher alcohols [6, 35, 64]. The XPS results in Table 4 show that the surface Rh is in a non stoichiometric oxidation state, implying the presence of $Rh^{+}/Rh^{0}$ pairs at the interface of the Rh clusters with LZ. The coupling between ionic and atomic Rh in presence of La and Zr ions found in the LZ crystal lattice structure may act as promoters for C-C coupling and subsequently for the formation of higher alcohols [6, 35, 64-65].

The LZ support appears to have two important roles in the reaction process: (a) it provides centers for the Rh catalyst through its basic La component on the surface, and (b) the interface between Rh and LZ helps in decreasing the reducibility of Rh on the surface, apparently producing the sort of $Rh^{+}/Rh^{0}$ sites needed for higher oxygenate formation.

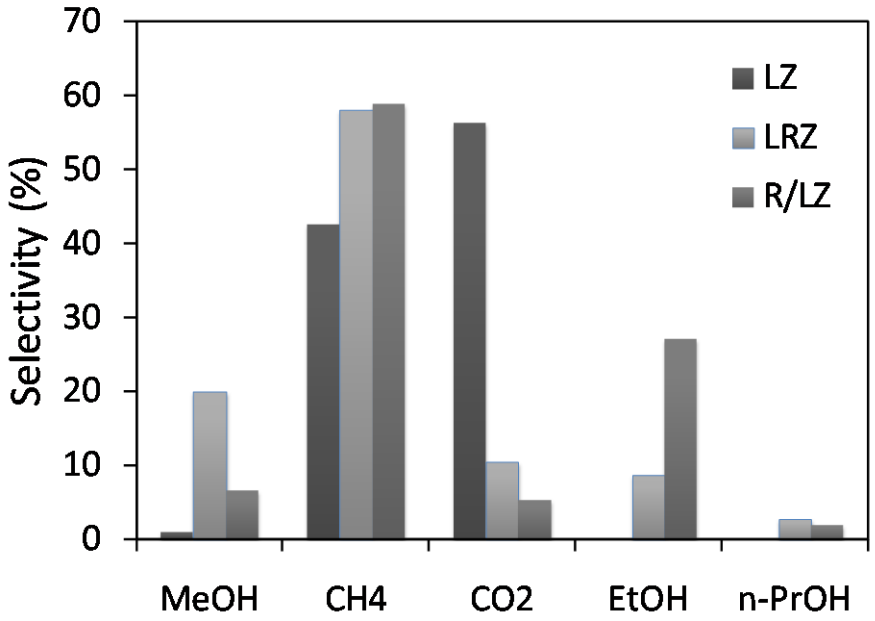


Figure 7. Catalytic carbon-based selectivity towards methanol, methane, $CO_2$, ethanol and n-propanol at WHSV of 15000 $cm^3/g/h$, in the syngas mixture of $H_2/CO=2$ and at 2.9 MPa.

The selectivities shown in Figure 7 suggest that the reaction mechanism on LRZ and on R/LZ catalysts maybe different. Figure 7 also shows that the oxygenate product distribution on LRZ catalyst follows Anderson-Schulz-Flory (ASF) chain growth mechanism. This could be due to the high reducibility of Rh on the surface (mainly $Rh^o$). On the other hand, when the Rh oxidation state on the catalyst surface became with a more ionic nature, the reaction mechanism changes and CO insertion is kinetically faster than CO dissociation, leading to higher ethanol selectivity. Interestingly, the reaction mechanism for methane formation could be independent from alcohol formation for these two catalyst types since the selectivity remained constant.

Gysling et al. [30] showed that the mechanism of methanol formation is different from ethanol and acetaldehyde on $LaRhO_3$. At high reaction temperature (> 300$^oC$) the $LaRhO_3$ activity favors $C_2$ oxygenates while at low reaction temperatures (< 300 $^oC$) methanol selectivity increases. A similar result was observed on LRZ in the present work. LRZ has a minor secondary $LaRhO_3$ phase present which seems to play an important role in catalyst selectivity. At 280$^oC$, LRZ favors methanol formation over higher alcohols. Gysling et al. also show that the Rh in $LaRhO_3$ can be reduced to form $Rh^0$, which they claim as the active Rh species. Additionally, the difference in activation energy between methanol (28±2 kcal/mole) and higher oxygenates 16±3 kcal/mol [29] implies that higher oxygenates originated from the common $CH_x$ unit formed by hydrogenation of dissociatively adsorbed CO while methanol is formed by hydrogenation of associatively adsorbed CO. The observed selectivity is the result of competition between CO insertion and hydrogenation of $CH_x$ species on the surface (Figure 8).

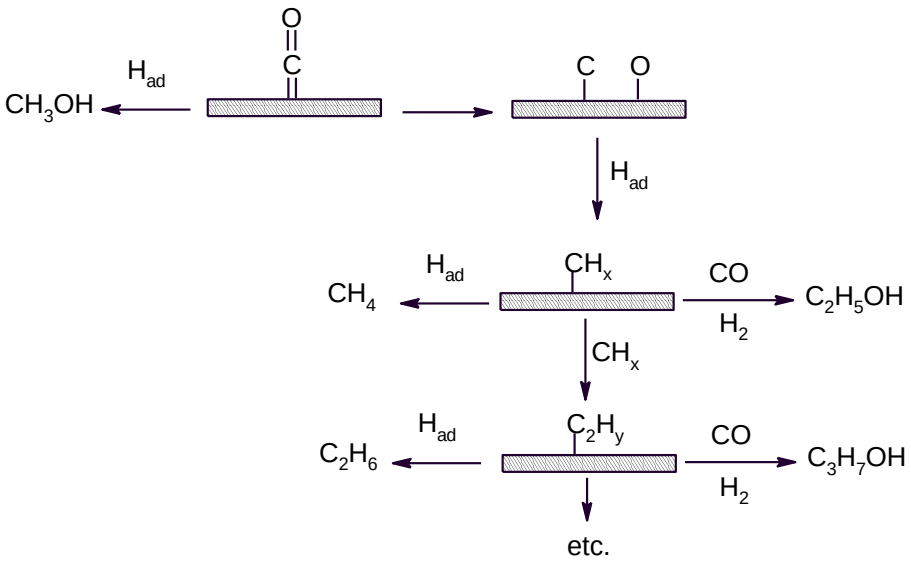


Figure 8. Proposed reaction pathways on Rh-based catalyst surface leading to hydrocarbons and higher oxygenates during CO hydrogenation reaction.

## 4.0 Conclusion

Lanthanum zirconate pyrochlores with rhodium either substituted within the lattice (LRZ) or supported on a pure lanthanum zirconate (R/LZ) were prepared using a modified Pechini method. The catalytic selectivity of these materials towards CO hydrogenation into alcohols shows that the nature of Rh oxidation state on the catalyst surface plays an essential role in determining the product selectivity. Atomically adjacent metallic and oxidized rhodium sites and their relative proportion determine the selectivity to methanol or ethanol as the main product. TPR, $H_2$ pulse chemisorption and XPS analysis show that surface rhodium in the pyrochlore structure (LRZ) is significantly more reducible than rhodium supported on an LZ pyrochlore support (R/LZ). The more metallic Rh sites in LRZ favor the methanol formation compared to higher alcohols, with the alcohol product distribution following the ASF chain growth mechanism. However, R/LZ has mainly ionic $Rh^+$ surface species and shows far greater ethanol selectivity.

## 5.0 Acknowledgements

Funding provided by NETL-Fuels program, Research and Engineering Support (RES), Contract No. FE0004000.We gratefully acknowledge David Berry, Daniel Haynes, and Mark Smith for useful discussions, Frank Thomas for reactor setup, and Kimberly Carter and Jinesh Jain for ICP analysis.

## 6.0 References

1. J.J. Spivey and A. Egbebi, Chem. Soc. Rev., 36 (2007) 1514.

2. H.-B. Zhang, X.-L. Liang, X. Dong, H.-Y. Li, and G.-D. Lin, Catal. Surv. Asia, 13 (2009) 41.
3. J. He and W.-n. Zhang, J. Zhejiang Univ., Sci., A, 9 (2008) 714.
4. S. Mawson, M.S. McCutchen, P.K. Lim, and G.W. Roberts, Energy Fuels, 7 (1993) 257.
5. Y. Wang, J. Li, and W. Mi, React. Kinet. Catal. Lett., 76 (2002) 141.
6. F.G.A. Van den Berg, J.H.E. Glezer, and W.M.H. Sachtler, J. Catal., 93 (1985) 340.
7. H. Trevino, G.-D. Lei, and W.M.H. Sachtler, J. Catal., 154 (1995) 245.
8. M.F.H. van Tol, A. Gielbert, and B.E. Nieuwenhuys, Applied Surface Science, 67 (1993) 166.
9. K. Tominaga, Y. Sasaki, M. Saito, K. Hagihara, and T. Watanabe, J. Mol. Catal., 89 (1994) 51.
10. M.R. Gogate and R.J. Davis, Catal. Commun., 11 (2010) 901.
11. A. Boffa, C. Lin, A.T. Bell, and G.A. Somorjai, J. Catal., 149 (1994) 149.
12. G. Chen, C.-Y. Guo, Z. Huang, and G. Yuan, Chemical Engineering Research and Design, 89 (2011) 249.
13. M.A. Haider, M.R. Gogate, and R.J. Davis, J. Catal., 261 (2009) 9.
14. H.M. Yin, Y.J. Ding, H.Y. Luo, W.M. Chen, and L.W. Lin, Stud. Surf. Sci. Catal., 147 (2004) 421.
15. A. Erdöhelyi and F. Solymosi, J. Catal., 84 (1983) 446.
16. R.P. Underwood and A.T. Bell, Appl. Catal., 21 (1986) 157.
17. J. Stubenrauch and J.M. Vohs, Catal. Lett., 47 (1997) 21.
18. J. Wang, Q. Zhang, and Y. Wang, Catal. Today, 171 (2011) 257.

19. M.E. Rivas, J.L.G. Fierro, M.R. Goldwasser, E. Pietri, M.J. Pérez-Zurita, A. Griboval-Constant, and G. Leclercq, Applied Catalysis A: General, 344 (2008) 10.
20. D. Jiang, Y. Ding, Z. Pan, X. Li, G. Jiao, J. Li, W. Chen, and H. Luo, Appl. Catal., A, 331 (2007) 70.
21. Y. Choi and P. Liu, J Am Chem Soc, 131 (2009) 13054.
22. V.R. Surisetty, A.K. Dalai, and J. Kozinski, Energy Fuels, 24 (2010) 4130.
23. X. Mo, J. Gao, N. Umnajkaseam, and J.G. Goodwin, J. Catal., 267 (2009) 167.
24. Y. Du, D. Chen, and K. Tsai, Appl. Catal., 35 (1987) 77.
25. A. Egbebi, V. Schwartz, S.H. Overbury, and J.J. Spivey, Catal. Today, 149 (2010) 91.
26. H. Orita, S. Naito, and K. Tamaru, Chem. Lett., (1983) 1161.
27. M. Gupta, M.L. Smith, and J.J. Spivey, ACS Catalysis, 1 (2011) 641.
28. M. Ojeda, M.L. Granados, S. Rojas, P. Terreros, F.J. Garcia-Garcia, and J.L.G. Fierro, Appl. Catal., A, 261 (2004) 47.
29. P.R. Watson and G.A. Somorjai, J. Catal., 74 (1982) 282.
30. H.J. Gysling, J.R. Monnier, and G. Apai, J. Catal., 103 (1987) 407.
31. Z. Li, Y. Fu, J. Bao, M. Jiang, T. Hu, T. Liu, and Y.n. Xie, Appl. Catal., A, 220 (2001) 21.
32. G. Van der Lee, B. Schuller, H. Post, T.L.F. Favre, and V. Ponec, J. Catal., 98 (1986) 522.
33. H. Wang, J. Liu, J. Fu, J. Cai, H. Zhang, and Q. Cai, J. Nat. Gas Chem., 2 (1993) 13.
34. A. Takeuchi and J.R. Katzer, The Journal of Physical Chemistry, 86 (1982) 2438.
35. Y. Wang, H. Luo, D. Liang, and X. Bao, J. Catal., 196 (2000) 46.

36. A. Kiennemann, R. Breault, J.P. Hindermann, and M. Laurin, J. Chem. Soc., Faraday Trans. 1, 83 (1987) 2119.

37. F. Tietz, A. Schmidt, and M. Zahid, Journal of Solid State Chemistry, 177 (2004) 745.

38. A. Majid, J. Tunney, S. Argue, D. Wang, M. Post, and J. Margeson, Journal of Alloys and Compounds, 398 (2005) 48.

39. A.W. Burton, K. Ong, T. Rea, and I.Y. Chan, Microporous and Mesoporous Materials, 117 (2009) 75.

40. E.P. Barrett, L.G. Joyner, and P.P. Halenda, J Am Chem Soc, 73 (1951) 373.

41. Y. Tong, Y. Wang, Z. Yu, X. Wang, X. Yang, and L. Lu, Materials Letters, 62 (2008) 889.

42. M.A. Subramanian, G. Aravamudan, and G.V. Subba Rao, Progress in Solid State Chemistry, 15 (1983) 55.

43. M.A. Subramanian, G. Aravamudan, and G.V. Subba Rao, Progress in Solid State Chemistry, 15 (1983) 55.

44. J.S. Gardner, M.J.P. Gingras, and J.E. Greedan, Reviews of Modern Physics, 82 (2010) 53.

45. T. Su, H. Jiang, and H. Gong, Journal of Solid State Chemistry, 184 (2011) 2601.

46. T. Weon-Pil, Materials Science and Engineering: B, 103 (2003) 83.

47. V. Abdelsayed, A. Aljarash, M.S. El-Shall, O.Z.A. Al, and A.H. Alghamdi, Chem. Mater., 21 (2009) 2825.

48. A.R. Siamaki, A.E.R.S. Khder, V. Abdelsayed, M.S. El-Shall, and B.F. Gupton, J. Catal., 279 (2011) 1.

49. M.S. El-Shall, V. Abdelsayed, A.E.R.S. Khder, H.M.A. Hassan, H.M. El-Kaderi, and T.E. Reich, J. Mater. Chem., 19 (2009) 7625.

50. D.J. Haynes, D.A. Berry, D. Shekhawat, and J.J. Spivey, Catal. Today, 136 (2008) 206.

51. D.L. Hoang and H. Lieske, Thermochimica Acta, 345 (2000) 93.

52. D.J. Haynes, D.A. Berry, D. Shekhawat, and J.J. Spivey, Catal. Today, 136 (2008) 206.

53. H.Y. Luo, W. Zhang, H.W. Zhou, S.Y. Huang, P.Z. Lin, Y.J. Ding, and L.W. Lin, Appl. Catal., A, 214 (2001) 161.

54. B.J. Wuensch, K.W. Eberman, C. Heremans, E.M. Ku, P. Onnerud, E.M.E. Yeo, S.M. Haile, J.K. Stalick, and J.D. Jorgensen, Solid State Ionics, 129 (2000) 111.

55. G.C. Bond and D.G. Richards, Appl. Catal., 28 (1986) 303.

56. S. Suhonen, M. Valden, M. Hietikko, R. Laitinen, A. Savimäki, and M. Härkönen, Applied Catalysis A: General, 218 (2001) 151.

57. J.F. Múnera, S. Irusta, L.M. Cornaglia, E.A. Lombardo, D. Vargas Cesar, and M. Schmal, J. Catal., 245 (2007) 25.

58. Y.V. Larichev, O.V. Netskina, O.V. Komova, and V.I. Simagina, Int. J. Hydrogen Energy, 35 (2010) 6501.

59. Y. Wang, Z. Song, D. Ma, H. Luo, D. Liang, and X. Bao, J. Mol. Catal. A Chem., 149 (1999) 51.

60. D.E. Newbury, D.C. Joy, P. Echlin, C.E. Fiori, and J.I. Goldstein, *Advanced Scanning Electron Microscopy and X-Ray Microanalysis*. (1986). 454 pp.

61. D. Briggs, M.P. Seah, and Editors, *Practical Surface Analysis by Auger and X-ray Photoelectron Spectroscopy*. (1983). 533 pp.

62. A. Zangwill, *Physics at Surfaces*. (1988). 454 pp.

63. P. Forzatti, E. Tronconi, and I. Pasquon, Catal. Rev. - Sci. Eng., 33 (1991) 109.

64. G. Van der Lee and V. Ponec, J. Catal., 99 (1986) 511.

65. Z.-r. Li, Y.-l. Fu, and M. Jiang, Applied Catalysis A: General, 187 (1999) 187.